# Theoretical Proposal of a Multiphysical Quantity Measurable Sensor With Coexistence of Absorption and Transmission

Tao Zhang, Yu Ma, and Hai-Feng Zhang

Abstract—In this article, a 1-D periodic photonic crystals (PCs) cell structure composed of indium antimonide (InSb) and common dielectrics is proposed for the application of detection of temperature and magnetic fields with an absorption peak in the transmission band (APITB), and the sensing properties are also studied with the sensitivity (S) of 1.519 THz/T (detection range: 1–4.5 T) and 0.081 THz/K (detection range: 220–290 K) for the measurement of magnetic and temperature fields with coexistence of absorption and transmission. Based on the tunability of APITB, the general structure of PCs with InSb is designed by stacking different magnetic fields of cell structure giving rise to the realization of a transmission window in the absorption band (TWIAB) due to each joining configuration of APITB. Besides, TWIAB with different distributions in THz regime can be obtained by changing the magnetic fields. Moreover, through the analysis of its sensing performance, it can be concluded that the proposed splicing structure can achieve a wide range of magnetic field detection from 0.6 to 5.1 T in the THz regime with a sensitivity of 1.85296 THz/T. These calculated results can assist in the multiphysical quantity measurement of magnetic and temperature fields with a coexisting absorption–transmission conversion.

Index Terms—Co-existing modulation of absorption and transmission, indium antimonide (InSb), photonic crystals (PCs), transfer matrix method (TMM), ultra-wideband absorption.
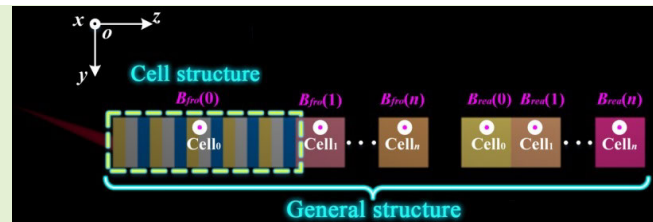
I. INTRODUCTION

PHOTONIC crystals (PCs) [1], [2] are artificial structures, which are composed of a periodic arrangement of dielectrics with different refractive indices and play a great significant role in regulating the propagation of electromagnetic (EM) waves. An important property of PCs is photonic band gaps [3], [4] where the propagation of EM waves is prohibited. Utilizing the properties of PCs, the researchers found that different materials combined with a variety of topological structures can realize the particular manipulation of EM waves, such as nonreciprocal transmission [5], [6], polarization separation [7], [8], perfect absorption [9], [10], and so on. Due to the unique EM properties and perfect theoretical basis of PCs, growing studies on the theory of PCs for sensing also occur, such as surface plasmon resonance sensors [11], [12], and PC

fiber sensors [13], [14]. PCs located defect mode resonance [15], [16] is also applied to the detection of sensors. Sensors are categorized in terms of physical quantities measured, such as temperature sensors [17], [18], refractive index sensors [19], [20], magnetic field sensors [21], [22], biosensors [23], [24], and multiphysical quantity measurable sensors [25], [26]. Multiphysical quantity measurable sensors have become a research direction of interest to researchers in recent years due to their greater convenience compared to sensors that measure a single physical quantity and provide greater degrees of freedom for the sensor. Amiri et al. [25] investigated the tricore PC microstructure fiber for simultaneous measurement of salinity and temperature of water substances. Moreover, Wan et al. [26] also proposed a sensor capable of multiphysical quantity detection. The presented sensor can be applied to measure four physical quantities simultaneously, including magnetic induction intensity, plasma density, refractive index, and incident light angle. However, PCs designed sensors based on photonic band gaps measure the transmission in reflection, so there are no PCs sensors with absorption transmission coexistence at present. Although, Ma et al. [27] study the absorption peak in the transmission band (APITB) explained by Brewster's law, this phenomenon has not yet been applied to the field of sensors, especially in measuring the transmission window in the absorption band (TWIAB), which is still a

research gap in the sensor. Therefore, combining APITB with sensors and expanding it to TWIAB measurement is one of innovative works in this article.

The selection of materials for the configuration of PCs is crucial to make a difference in the EM properties, which is of some significance to sensing performance. Considering the tunability of PCs for EM waves, more special materials are introduced into PCs, for instance, plasma [28], metal [29], graphene [30], superconductor [31], and semiconductor [32]. Indium antimonide (InSb) [33] is a semiconductor material that has attracted more attention due to its magnetic tunability, which is still of enormous interest to both material scientists and device engineers for its optical properties. Ghafari et al. [34] designed a temperature sensor with the characteristics of tunability of InSb and its temperature sensitivity. In this article, we will theoretically investigate the tunable properties of 1-D PCs with InSb for sensing.

In this study, the properties of 1-D PCs with semiconductor InSb for the application of sensors capable of measuring multiple physical quantities are discussed. The APITB and TWIAB can be realized in our work. In addition, the effects of the magnetic field and temperature on the performances of APITB are investigated by the transfer matrix method (TMM), and the sensing performance is also researched. The correctness of the results for the proposed structure is checked by giving the electric field distributions at critical frequencies. The simulated results show that the characteristics of APITB and TWIAB can provide the possibility for the magnetic field and temperature sensor and realization of conversion and coexistence of absorption and transmission in the terahertz (THz) regime. The APITB structure was first designed to enable the detection of temperature and magnetic induction strength by combining the Brewster's law with the sensitivity of $S = 1.51905$ THz/T and $S = 0.08062$ THz/K, and then considering the convenience of adjusting the magnetic field compared to the temperature field, the cell structures with different magnetic induction strengths were stacked so that plenty of absorption peaks were spliced into an absorption band. The discrete points of continuous magnetic induction strength are the transmission windows, and thus TWIAB is realized with the sensitivity of $S = 1.85296$ THz/T, higher than that of APITB, but the quality factor of TWIAB decreases significantly due to the stacked structures. Simulation data show that TWIAB can cover the detection of the entire THz regime. There is little literature on sensors with the TWIAB, which our work can promote the measurement in the field of sensors, and the proposed structure has the characteristics of measuring multiple physical quantities, offering great potential for application in multiphysical quantity sensors. Furthermore, the properties of the APITB and TWIAB can provide ideas for switchable absorption–transmission window signal modulators, radomes, and optical shield.

II. THEORETICAL MODEL AND METHOD

The schematic illustration of one cell structure consisting of 1-D PCs with semiconductor InSb is described in Fig. 1(a), which offer realization of APITB. One unit periodic structure is shown in Fig. 1(b), a component part of one cell structure,
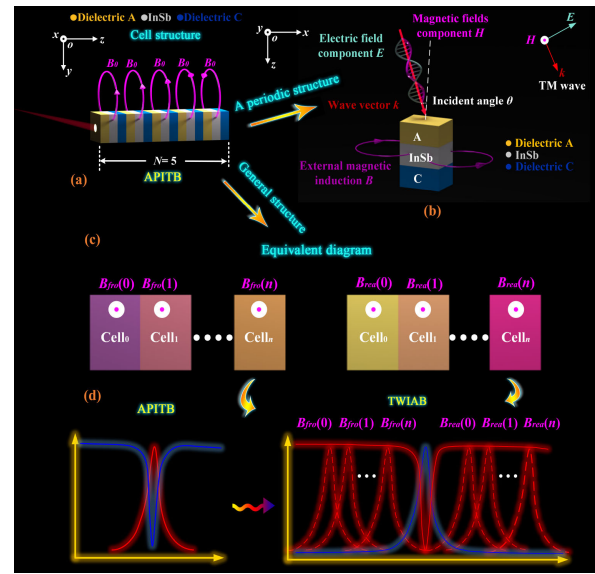

Fig. 1. (a) Schematic illustration of one cell structure consisting of 1-D PCs with semiconductor InSb, realizing coexisting modulation of absorption and transmission APITB with the same magnetic field B_0 for the detection of magnetic and temperature fields. (b) Schematic illustration of one unit periodic structure composing the structure of the APITB. (c) Equivalent diagram of the general structure that can achieve TWIAB mechanism with the different magnetic field distribution from $B_{\text{fro}}(0)$–$B_{\text{fro}}(n)$ to $B_{\text{rea}}(0)$–$B_{\text{rea}}(n)$. (d) Waveform schematic for forming APITB and TWIAB.

composed of the arrangement of "A, InSb, C" sequence, where the dielectric A ($n_A = (51)^{1/2}$) and C ($n_C = 1$) are two common dielectrics with thicknesses of $d_A = 1.6$ μm and $d_C = 6.4$ μm, respectively. Silver dielectric layer represents InSb. The thickness of layer InSb is $d_{\text{InSb}} = 50$ nm. The cell structure shown in Fig. 1(a) for the provision of the APITB mechanism is made up of five periodic configurations ($N = 5$) given in Fig. 1(b), and the magnetic induction intensity applied to the semiconductor material InSb is the same with constant $B_0 = 2$ T. The general structure for the TWIAB mechanism is plotted in Fig. 1(c), and the equivalent diagram displays that the general structure is composed of cell structures controlled by different magnetic fields B consisting of magnetic field distribution of the front B_{fro} and rear B_{rea} section, where the front and rear magnetic field distributions (B_{fro}, B_{rea}) are both Arithmetic progression. Each change of Arithmetic progression represents one cell structure shown in Fig. 1(a). Assuming the magnetic field distribution is 0.1–3 T for B_{fro}, the expression of magnetic fields is $B_{\text{fro}}(n) = 0.1 + 0.01n$ ($n = 0$–290). The expression indicates that the magnetic induction intensity applied to Cell$_0$ is 0.1 T, and that to Cell$_1$ is 0.11 T until that to Cell$_n$ is 3 T. The magnetic field applied to the rear of the structure is similar. In the proposed design, the cell structure is responsible for APITB, while the whole structure contributes the phenomenon of the TWIAB. Waveform schematic is drawn in Fig. 1(d) to visualize the formation process of TWIAB. One cell structure provides APITB. Considering the convenience of adjusting magnetic induction strength compared with temperature field, cell structures that generate absorption peaks at different frequencies through splicing can result in the appearance of absorption band, and then a transmission window will be formed at the discrete

point of continuous magnetic induction strength, which can realize TWIAB.

For the proposed configuration of the topological structure, the reflectance and transmittance can be computed by TMM [35]. The derivation process is as follows. The dielectric function $\varepsilon_{\text{InSb}}$ is anisotropy, and the following expression can be derived [36]:

$$\varepsilon_{\text{InSb}} = \begin{bmatrix} \varepsilon xx & 0 & 0 \\ 0 & \varepsilon yy & -\varepsilon yz \\ 0 & \varepsilon yz & \varepsilon zz \end{bmatrix} \quad (1)$$

where the formula of tensor elements can be written as [36]

$$\varepsilon_{xx} = \varepsilon_\infty - \varepsilon_\infty \frac{\omega_p^2}{\omega(\omega + \gamma i)} \quad (2)$$

$$\varepsilon_{yy} = \varepsilon_\infty - \varepsilon_\infty \frac{\omega_p^2(\omega + \gamma i)}{\omega[(\omega + \gamma i)^2 - \omega_c^2]} \quad (3)$$

$$\varepsilon_{yz} = \varepsilon_\infty \frac{i\omega_p^2\omega_c}{\omega[(\omega + \gamma i)^2 - \omega_c^2]} \quad (4)$$

where ε_∞ stands for the high-frequency limit permittivity, whose value is 15.68, γ is the collision frequency of carriers and set as 0.04 π THz, and ω_p denotes the plasma frequency that can be written as [36]

$$\omega_p = (Ne^2/\varepsilon_0 m^*)^{1/2} \quad (5)$$

where N refers to intrinsic carrier density and e is the electron charge, and ε_0 denotes the free space permittivity. m^* describes the effective mass of the carrier for InSb and $m^* = 0.015\, m_e$. m_e is the mass of an electron. The dielectric property of InSb is greatly influenced by N, which is related to temperature Te and can be written as [36]

$$N = 5.76 \times 10^{20} Te^{1.5} e^{[-0.26/(2 \times 8.625 \times 10^{-5} \times Te)]} \quad (6)$$

where ω_c is the cyclotron frequency, which is affected by the external magnetic fields, and the specific expression is [36]

$$\omega_c = eB/m^*. \quad (7)$$

Finally, the effective dielectric constant of the InSb layer for the TM wave can be given as [36]

$$\varepsilon_{\text{TM}} = (\varepsilon_{yy}^2 - \varepsilon_{yz}^2)/\varepsilon_{yy}. \quad (8)$$

With the expression of effective dielectric constant of InSb, the transfer matrix of InSb layer can be written as [36] (9), as shown at the bottom of the next page, $k_x = \omega/c(\varepsilon_{\text{TM}})^{1/2}\sin\theta_{\text{InSb}}$, $k_z = \omega/c(\varepsilon_{\text{TM}})^{1/2}\cos\theta_{\text{InSb}}$, θ_{InSb} indicates the incident angle of the InSb layer, $\eta = (\varepsilon_0/\mu_0)^{1/2}(\varepsilon_{\text{TM}})^{1/2}/\cos\theta_{\text{InSb}}$.

Compared with InSb layer, the transfer matrix of ordinary dielectric layer is relatively simple [35]

$$M_{i=A,C} = \begin{bmatrix} \cos\delta_i & -\frac{j}{\eta_i}\sin\delta_i \\ -j\eta_i\sin\delta_i & \cos\delta_i \end{bmatrix} \quad (10)$$

where $\eta_i = n_i/\cos\theta_i$, $\delta_i = (2\pi/\lambda)n_i d_i \cos\theta_i$, n_i signifies the refractive index of layer i, d_i, and θ_i indicate the thickness and incident angle of layer i, respectively. λ corresponds to the wavelength of the EM wave.

After EM waves pass through the cell structure of proposed 1-D PCs with semiconductor InSb, the transmission matrix can be expressed as [35]

$$M = (M_A \times M_P \times M_B)^5 = \begin{pmatrix} m_{11} & m_{12} \\ m_{21} & m_{22} \end{pmatrix}. \quad (11)$$

The reflectance, transmittance, and absorptance of EM waves can be signified as [35]

$$\text{Res} = |r|^2, \text{Trs} = |t|^2, \text{Abs} = 1 - \text{Res} - \text{Trs} \quad (12)$$

where r stands for the reflection coefficient, and t denotes the transmission coefficient [35]

$$r = \frac{(m_{11} + m_{12}\eta_0)\eta_0 - m_{21} - m_{22}\eta_0}{(m_{11} + m_{12}\eta_0)\eta_0 + m_{21} + m_{22}\eta_0} \quad (13)$$

$$t = \frac{2\eta_0}{(m_{11} + m_{12}\eta_0)\eta_0 + m_{21} + m_{22}\eta_0} \quad (14)$$

where $\eta_0 = n_0/\cos\theta_0$(TM wave), n_0 is the refractive index of air and θ_0 is the incident angle of EM waves.

III. ANALYSIS AND DISCUSSION

A. Features of the Cell Structure

The analysis of absorptance and transmission curves is presented in Fig. 2 with external magnetic fields and temperature: $Te = 220$ K, $B = 2$ T. Fig. 2(a) is the transmittance graph, from which it can be seen that there is a transmission band with the stable frequency in the angle range of 78°–84°, only one defect at 4.96 THz. From the absorptance graph in Fig. 2(b), we can understand that it is an absorption defect. Besides, the numerical simulation exhibited by Fig. 2(c) shows that absorption peaks of the proposed cell structure at different incident angles mainly distribute at 4.96 THz, which is angle stable. In combination with Fig. 2(a) and (b), it can be found that the APITB within a certain angle range can be achieved for the proposed cell structure. It can be seen from the chart that the EM waves are transmitted by the structure except an absorption peak with a large value of 0.92 at 4.96 THz.

These conclusions can be explained from two aspects (absorption defect and broadband transmission). First, the absorption defect can be explained as InSb is a dissipative medium because of its plasma frequency ω_p and collision frequency γ. The collision between particles will lead to the loss of EM waves into the internal energy of InSb. In addition, ω_c is produced under the effect of the magneto-optical Voigt effect [37], [38], which can enhance the collision. In the following discussion of parameters, it can be known that EM waves of the frequency corresponding to the great change in the refractive index of InSb (n_{TM}) are more easily absorbed. Therefore, the absorption defect can be found in the studied frequency band for the proposed structure with InSb. Moreover, the discuss of energy loss is given in the supplemental material.

Second, the generation of transmission band results from Brewster's angle. Based on Brewster's law, the reflected wave propagating in the dielectric at Brewster's angle is linearly polarized, perpendicular to the incident plane and transmitted light. From the coordinate relationship between TE and TM waves, it can be understood that the reflected wave propagates
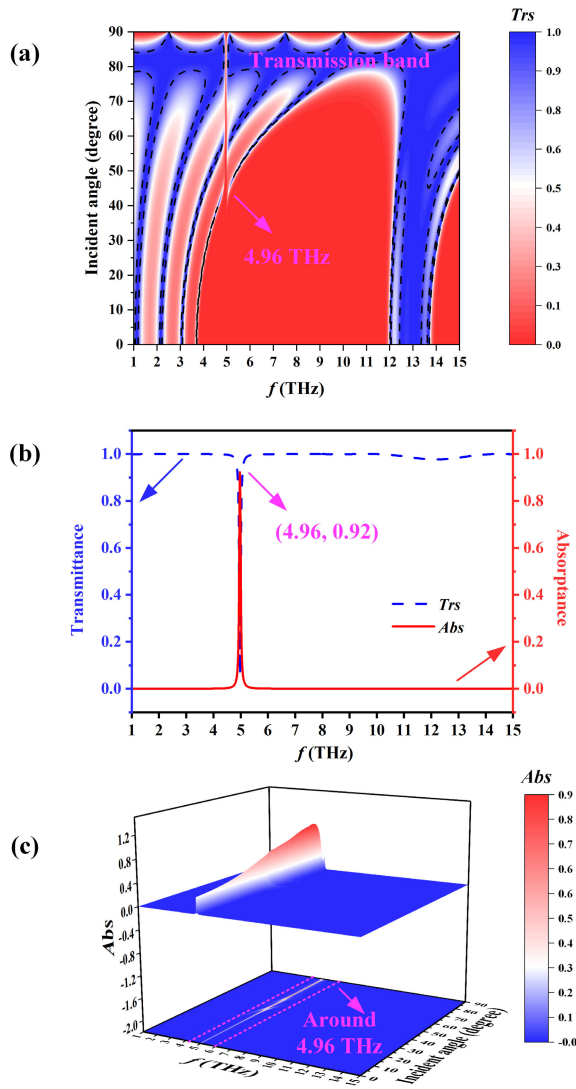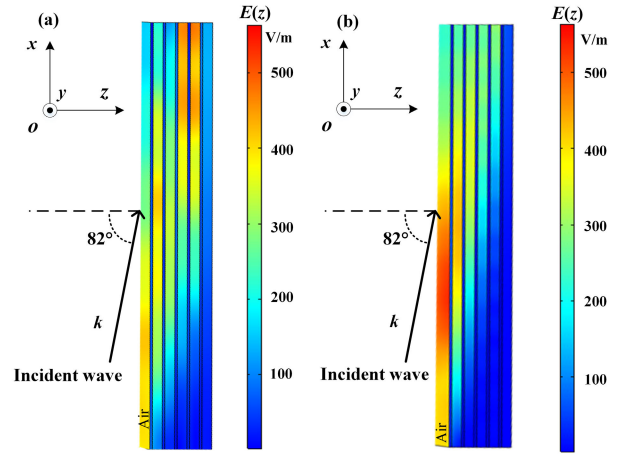
Fig. 3. Diagrams of electric field distributions for the proposed cell structure with simulation of (a) transmission (15 THz) and (b) absorption (4.96 THz).

Fig. 2. (a) Diagrams of transmittance Trs at different frequencies f with varied incident angles θ. (b) Diagrams of APITB at different frequencies f with incident angles θ of $\theta = 82°$ when $Te = 220$ K, $B = 2$ T. (c) Diagrams of absorptance Abs for the proposed structure, showing that absorption peaks mainly distribute at 4.96 THz with different incident angles θ.

to a common effective dielectric constant. According to the effective dielectric constant theory [39]

$$\varepsilon_{\text{eff}} = \frac{\varepsilon_C d_C + \varepsilon_{\text{InSb}} d_{\text{InSb}}}{d_C + d_{\text{InSb}}}. \tag{16}$$

It can be obtained that $\varepsilon_{\text{eff}} \approx 1.06$. Finally, Brewster's angle can be calculated that $\theta_B = \arctan((51)^{1/2}/(1.06)^{1/2}) \approx 82°$. Because its value is equivalent, there is a broadband transmission of around 82°. In summary, the proposed cell structure makes it possible for the realization of APITB mechanism. Different Brewster's angles corresponding to the variation of n_A can be seen in supplemental material.

In order to explain the above phenomenon more intuitively and clearly, the diagrams of electric field distributions for the proposed cell structure are displayed in Fig. 3. It should be noted that the air layer is added to the top of the cell structure to ensure that the simulated results are more reasonable. It can be known from Fig. 2 that the frequency of 15 THz is the transmission frequency point, and absorption occurs at 4.96 THz. There is almost no EM wave with large incident angle in the cell structure far away from the incident direction (the lower right corner of the electric field diagrams). What is more noteworthy is that the energy of the EM wave passes through the cell structure obviously (the last layer is light blue) for the electric field diagram of the transmission frequency point [see Fig. 3(a)]. In contrast, the electric field color of the last layer is dark blue in case of absorption explaining that the energy of the EM wave is almost stored by the cell structure. These conclusion is in good agreement with those in Fig. 2.

B. Effects of B and Te on the Properties of APITB and n_{TM}

To investigate the effect of the applied magnetic fields and temperature on APITB, the absorptance curves of TM wave at

in the form of a TE wave, and the transmitted wave is a TM wave. From Snell's law and Brewster's law, Brewster's angle θ_B can be obtained

$$\theta_B = \arctan(n_2/n_1) \tag{15}$$

where n_1 and n_2 denote the refractive indices of different media. In the above formula, it is assumed that the incident wave is incident from medium 1 to 2. In this study, the refractive of normal dielectric A and C are $n_A = (51)^{1/2}$ and $n_C = 1$, respectively. It can be seen from the following that n_{TM} is around three except for the maximum value. Due to the thin thickness of InSb, InSb and medium C can be equivalent

$$M_{\text{InSb}} = \begin{bmatrix} \cos(k_z d_{\text{InSb}}) + \frac{k_x \varepsilon_{yz}}{k_z \varepsilon_{yy}} \sin(k_z d_{\text{InSb}}) & -\frac{j}{\eta}\left[1 + \left(\frac{k_x \varepsilon_{yz}}{k_z \varepsilon_{yy}}\right)^2\right]\sin(k_z d_{\text{InSb}}) \\ -j\eta \sin(k_z d_{\text{InSb}}) & \cos(k_z d_{\text{InSb}}) - \frac{k_x \varepsilon_{yz}}{k_z \varepsilon_{yy}} \sin(k_z d_{\text{InSb}}) \end{bmatrix}. \tag{9}$$
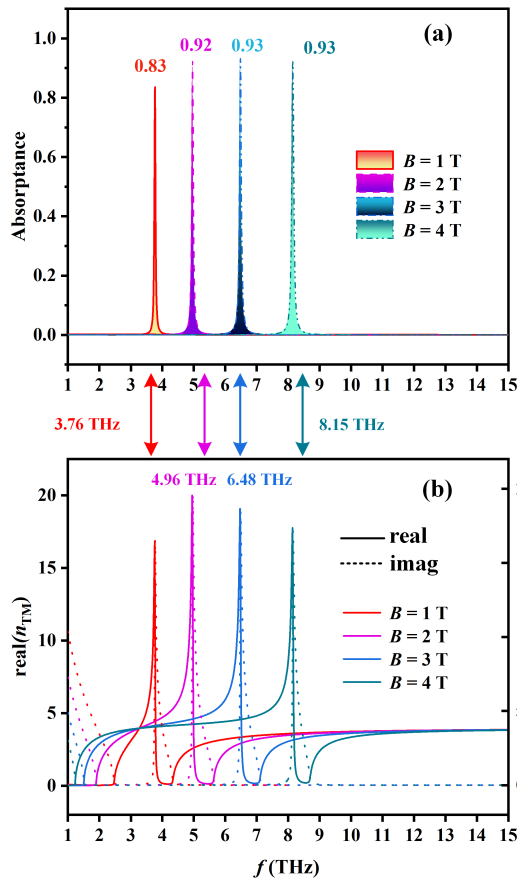
Fig. 4. Diagrams of (a) absorptances and (b) n_{TM} for the proposed cell structure at different magnetic fields B when $\theta = 82°$, $Te = 220$ K.

different B and Te is presented in Figs. 4 and 6, respectively. The variation of n_{TM} with two parameters is also given to indicate the internal reason for the influence of parameters on APITB.

The absorptances of TM wave and n_{TM} with different magnetic fields of $B = 1$ T, $B = 2$ T, $B = 3$ T, and $B = 4$ T are illustrated in Fig. 4. The absorption peak moves to the higher frequencies, and the peak value becomes large with the growing of B, similar to the trend of the real and imaginary curves of n_{TM} in Fig. 4(b). Compared Fig. 4(a) with (b), it should be noted that the position of frequency point which absorption appears is the same as the position where the real and imaginary parts of n_{TM} obtain the maximum values. We can infer that the magnetic field can regulate n_{TM} and then control the position of the absorption peak, which is related to the maximum frequency of n_{TM}. In addition, on the premise of ensuring high absorption, the transmittance around the absorption peak always maintains about 1, and the specific curve is similar to that shown in Fig. 2(b). These results also reveal that the APITB can be adjusted by B for the proposed cell structure. Therefore, eight groups of data ranging from $B = 1$ T to $B = 4.5$ T are chosen to express a linear fitting relationship between f and B in Fig. 5. To clearly show the sensing performance, the formula of sensitivity and figure of merit (FOM) is given. In this article, the sensitivity S in the frequency region is defined as the change rate of the frequency
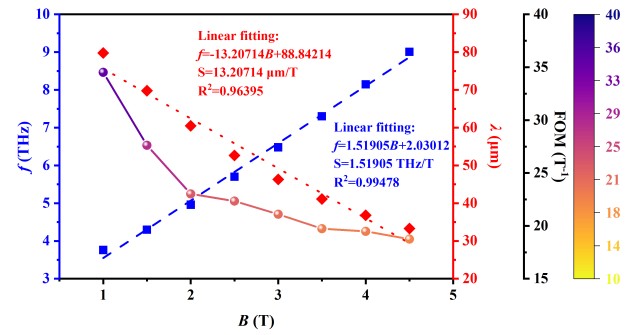

Fig. 5. Linear fitting relationship between frequency f and magnetic field B. The blue and red symbols in the diagram represent the relationship between the variety of absorption peaks and the magnetic field in the frequency domain and wavelength domain, respectively. The blue and red dotted lines are their corresponding linear fitting curves. The gradient curve represents the change of FOM with magnetic field B.

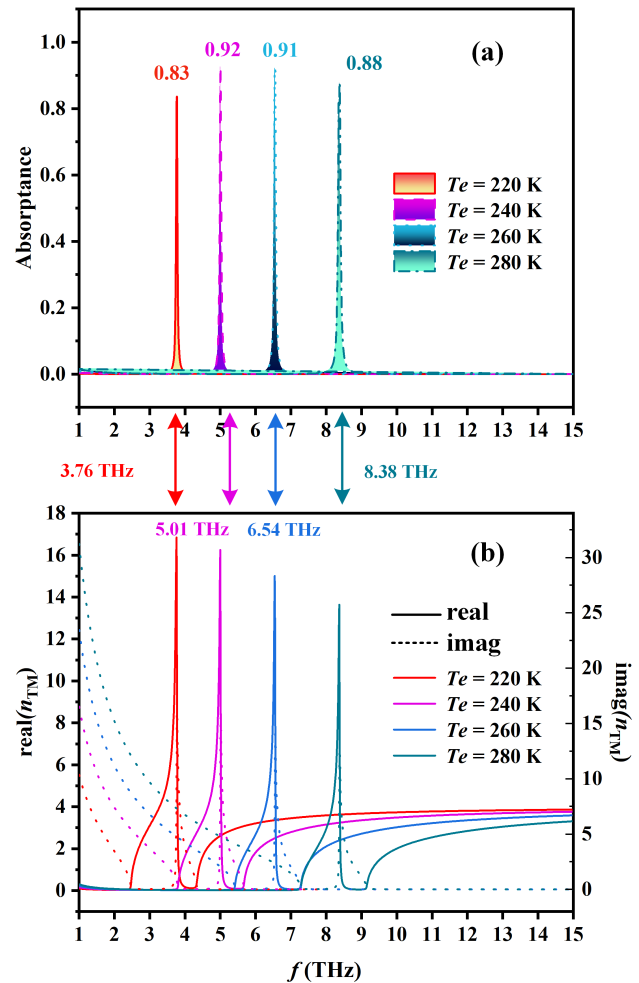**Fig. 6.** Diagrams of (a) absorptances of TM wave and (b) n_{TM} at different temperatures Te when $\theta = 82°$, $B = 1$ T.

with magnetic field or temperature [40], [41]

$$S = \frac{\Delta f}{\Delta B}, \text{ or } S = \frac{\Delta f}{\Delta Te}. \tag{17}$$

In addition, the corresponding expression of the FOM can be written as

$$\text{FOM} = \frac{S}{\text{FWHM}} \tag{18}$$

TABLE I
DETAILED DATA OF SENSOR PERFORMANCES FOR
THE VARIATION OF B

B (T)	f (THz)	Trs	FWHM (THz)	FOM (T^{-1})
1	3.76	0.83	0.044	34.52
1.5	4.30	0.89	0.055	27.62
2	4.96	0.92	0.066	23.02
2.5	5.70	0.93	0.068	22.34
3	6.48	0.93	0.072	21.10
3.5	7.30	0.93	0.077	19.73
4	8.15	0.93	0.078	19.48
4.5	9.01	0.91	0.081	18.75

TABLE II
DETAILED DATA OF SENSOR PERFORMANCES FOR
THE VARIATION OF Te

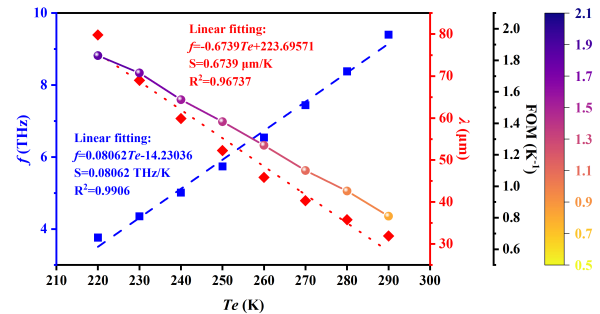| Te (T)	f (THz)	Trs	FWHM (THz)	FOM (°C^{-1})
220	3.76	0.83	0.044	1.83
230	4.35	0.89	0.047	1.72
240	5.01	0.92	0.052	1.55
250	5.74	0.94	0.057	1.41
260	6.54	0.91	0.064	1.26
270	7.44	0.90	0.073	1.10
280	8.38	0.88	0.083	0.97
290	9.40	0.83	0.099	0.81

where FWHM shows the full width at half maxima of the APITB.

Through data fitting, the linear fitting equation between f and B is $f = 1.519 B + 2.030$ with $R^2 = 0.99478$ and $S = 1.519$ THz/T with the average FOM of 23.32 T^{-1}. R^2 is very close to 1, indicating that the linear relationship between f and B is acceptable. Definitely, the APITB property of the cell structure can effectively detect the change in magnetic induction intensity. The detailed data are given in Table I. It can be seen from Table I that with the growth of values of B, the values of absorptance peak first increase and then decrease, and the selected data are the optimal solution in the frequency band.

The absorptances of TM wave and n_{TM} with different temperatures of $Te = 220$ K, $Te = 240$ K, $Te = 260$ K, and $Te = 280$ K are plotted in Fig. 6. It can be seen from Fig. 6(a) that the position of absorption peak moves to the higher frequencies when Te is increased. The peak value increases first and then decreases. The real and imaginary curves of n_{TM} are blue-shifted as Te is increased [shown in Fig. 6(b)]. It also can be noticed that the position of the absorption peak and the maximum values of real and imaginary parts of n_{TM} are identical, which are all situated at 3.76, 5.01, 6.54, and 8.38 THz, respectively, by contrasting Fig. 6(a) and (b). To manipulate the position of the absorption peak that is related to the maximum frequency of n_{TM}, n_{TM} should be adjusted by Te. Moreover, the value of transmittance of APITB also keeps around 1 with high absorptance in the middle band. These obtained results also indicate that the absorption peak of APITB can be tuned by Te for the proposed cell structure. The linear fitting relationship between f and Te is plotted in Fig. 7. After the data fitting method, the linear fitting equation of f and Te is $f = 0.081$ Te-14.230 with the sensitivity $S = 0.081$ THz/K and the linearity $R^2 = 0.99194$, which shows that level of the linear fitting between f and Te meets the challenge. The cell structure can be also applied in a sensor for temperature field detection. The detailed data can be seen in Table II, and the average FOM can be calculated as 1.33 °$^{-1}$C. Compared with previous work displayed in Table III, the proposed cell structure has high sensitivity and can realize the coexistence of absorption and transmission. In addition, the cell structure proposed in our work can measure temperature and magnetic fields simultaneously, which is more significantly convenient and efficient than other sensors measuring a single physical quantity.

Fig. 7. Linear fitting relationship between frequency f and temperature field Te. The blue and red symbols in the diagram represent the relationship between the variety of absorption peaks and the temperature in the frequency domain and wavelength domain, respectively. The blue and red dotted lines are their corresponding linear fitting curves. The gradient curve represents the change of FOM with different temperature Te.
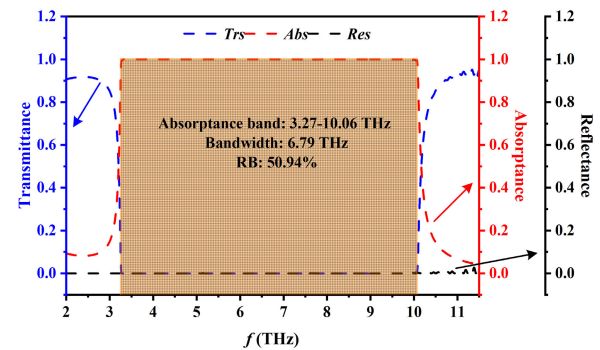
Fig. 8. Diagram of ultra-wideband absorption of TM wave for the proposed whole 1-D PCs structure with the stack of cell structures applied magnetic field B ranging from 0.1 to 5.1.

C. Analysis of TWIAB of the Whole Structure

The above analysis shows that the proposed cell structure can be applied to the generation of APITB mechanism. Assuming that cell structures resulting to different absorption peaks are spliced together, the broadband absorption composed of many single absorption peaks like Fig. 2(a) will be possible. Based on this, the whole 1-D PCs structure and its equivalent structure diagram as plotted in Fig. 1(c) and (d) is designed. The method of gradually increasing the magnetic field B is adopted to control the movement of the absorption peak, which is more convenient than temperature Te. The transmittance, reflectance, and absorptance for the proposed general structure are illustrated in Fig. 8.

The initial parameters are $d_A = 1.6$ μm, $d_C = 6.4$ μm, $d_{InSb} = 50$ nm, $n_A = (51)^{1/2}$, $n_C = 1$,

TABLE III
CHARACTERISTIC COMPARISON OF THE PROPOSED WORK WITH PREVIOUS WORK

| Refs.	Sensing materials	Coexistence of absorption and transmission	Measurable variables	Detection of temperature and magnetic fields	Detection range	Sensitivity	FOM
[26]	Plasma	No	4	No	0.2~2.6 T	1.41 GHz/T	30.65 /T
[42]	Ferrofluid	No	1	No	10~40 mT	0.073 nm/mT	No
[43]	Ethanol	No	1	No	45~75 °C	16.8142 nm/°C	No
[44]	Benzene	No	1	No	10~70 °C	110 nm/°C	5.5 /°C
[45]	Toluene	No	1	No	20~30 °C	11 nm/°C	No
Our work	InSb	Yes	2	Yes	1~4.5 T	1.51905 THz/T	23.32 /T
					220~290 K	0.08062 THz/K	1.33 /°C
					0.6~5.1 T	1.85296 THz/T	5.58 /T
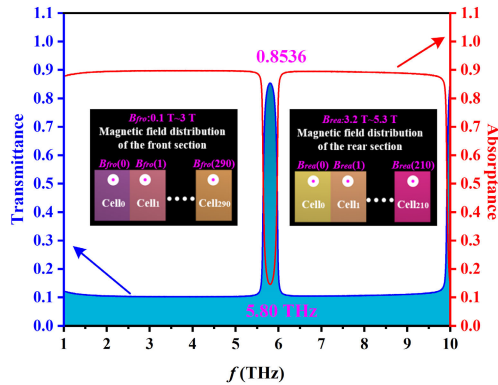
Fig. 9. Diagram of TWIAB for the proposed whole 1-D PCs structure with distribution of magnetic field ranging from $B_{\text{fro}} = 0.1 + 0.01n$ ($n = 0$–290) to $B_{\text{rea}} = 3.2 + 0.01n$ ($n = 0$–210).
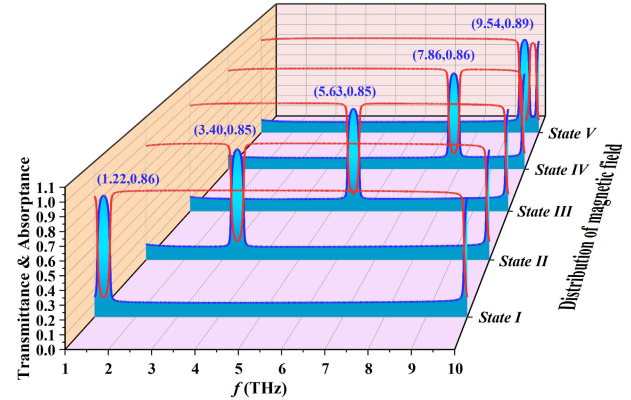

Fig. 10. Diagram of TWIAB for the proposed whole 1-D PCs structure with distribution of magnetic field ranging from State I to V in different frequency bands.

and $Te = 220$ K. B is applied to manipulate the position of absorption peak, whose value ranges from $B_0 = 0.1$ T to $B_n = 5.1$ T and the formula can be written as $B_n = (0.1 + 0.01n)$ T ($n = 0$–500, n is an integer). Specifically, the step length is 0.01 T and 501 such PC cells are stacked. It can be observed from Fig. 8 that the absorption phenomenon can be found in the designed whole structure, which lies in 3.27–10.06 THz (Abs $= 1$), and the bandwidth of ultra-wideband is 6.79 THz with relative bandwidth (RB) of 50.94%. The ultra-wideband absorption can be obtained by splicing successive absorption peaks. Supposing that some continuous absorption peaks are removed, which can be realized by skipping the B controlling these absorption peaks, the TWIAB will be obtained. Since the reflection coefficient is very small in the design structure, it can be ignored. The transmittance and absorptance of TM wave for the proposed whole 1-D PCs with TWIAB are given in Fig. 9.

The diagram of TWIAB is plotted in Fig. 9. The initial parameters are $d_A = 1.6$ μm, $d_C = 6.4$ μm, $d_{\text{InSb}} = 100$ nm, $n_A = (51)^{1/2}$, $n_C = 1$, $N = 20$, and $Te = 150$ K. It is defined that a series of magnetic fields applying in the cell structures to form the front absorption band is $B_{\text{fro}} = 0.1 + 0.01n$ ($n = 0$–290), and the rear is $B_{\text{rea}} = 3.2 + 0.01n$ ($n = 0$–210). The step length of B is 0.01 T, and the specific equivalent diagram explaining the TWIAB mechanism is shown in the internal illustration in Fig. 9. It can be observed from Fig. 9 that the value of absorptance is about 0.9 and the transmittance window distributes in 5.80 THz with the transmittance of 0.8536. Since the range of the magnetic fields in the front

and rear section is 0.1–3 T and 3.2–5.3 T, the magnetic field corresponding to the transmission peak in the middle of the absorption band in Fig. 9 is 3.1 T. Moreover, through data simulation, it is found that the TWIAB has strong nondeformation, and the movement of TWIAB at different frequencies can be realized by adjusting the magnetic field distribution. It is worth mentioning that TWIAB can be realized as long as it is in the ultra-wideband absorption band, theoretically covering the entire THz regime. Therefore, the feature of TWIAB can be applied to the detection of magnetic fields. The analysis of the sensing properties of TWIAB is described in detail below.

The diagram of TWIAB in different frequencies is plotted in Fig. 10. Different magnetic field distributions are defined as State I–V. State I $= \{B_{\text{fro}} = 0.1 + 0.01n$ ($n = 0$–40), $B_{\text{rea}} = 0.7 + 0.01n$ ($n = 0$–460)\}, State II $= \{B_{\text{fro}} = 0.1 + 0.01n$ ($n = 0$–160), $B_{\text{rea}} = 1.9 + 0.01n$ ($n = 0$–340)\}, State III $= \{B_{\text{fro}} = 0.1 + 0.01n$ ($n = 0$–280), $B_{\text{rea}} = 3.1 + 0.01n$ ($n = 0$–220)\}, State IV $= \{B_{\text{fro}} = 0.1 + 0.01n$ ($n = 0$–400), $B_{\text{rea}} = 4.3 + 0.01n$ ($n = 0$–100)\}, State V $= \{B_{\text{fro}} = 0.1 + 0.01n$ ($n = 0$–490), $B_{\text{rea}} = 5.2 + 0.01n$ ($n = 0$–10)\}. The transmittance window moves from 1.22 to 9.54 THz, and values of transmittance almost maintain about 0.85 with the variety of magnetic field distribution ranging from States I to V. However, when the transmission windows transfer, the absorption bands do not change and remain at 0.9. It is found that a controllable transmission band in ultra-wideband absorption can be realized, which has great significance for the coexistence of absorption and transmission.
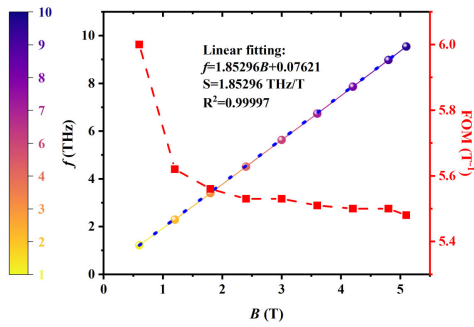
Fig. 11. Diagram of changing trend of TWIAB with different magnetic induction intensity B in frequency domain and its curve fitting spectrum. Gradual color curve and blue dotted line represent the trend and linear fitting curve of transmission frequency point with B, and the red line represents the change of FOM.

TABLE IV
DETAILED DATA OF SENSOR PERFORMANCES FOR THE DETECTION OF MAGNETIC FIELDS IN TWIAB MECHANISM

B (T)	B_{fro} (T)	B_{rea} (T)	f (THz)	Trs	FWHM (THz)	FOM (T^{-1})
0.6	0.1~0.5	0.7~5.3	1.22	0.86	0.31	6.00
1.2	0.1~1.1	1.3~5.3	2.29	0.85	0.33	5.62
1.8	0.1~1.7	1.9~5.3	3.40	0.85	0.33	5.56
2.4	0.1~2.3	2.5~5.3	4.51	0.85	0.34	5.53
3	0.1~2.9	3.1~5.3	5.63	0.85	0.34	5.53
3.6	0.1~3.5	3.7~5.3	6.73	0.86	0.34	5.51
4.2	0.1~4.1	4.3~5.3	7.86	0.86	0.34	5.50
4.8	0.1~4.7	4.9~5.3	8.98	0.87	0.34	5.50
5.1	0.1~5.0	5.2~5.3	9.54	0.89	0.34	5.48

Based on the above analysis of the magnetic controlled TWIAB, it can be seen that the peak value of the TWIAB corresponds to the middle missing B of the magnetic field distribution of the front and rear sections. Take State III as an example: the magnetic field distribution functions of the front and rear sections are, respectively, $B_{fro} = 0.1 + 0.01n$ ($n = 0$–280) and $B_{rea} = 3.1 + 0.01n$ ($n = 0$–220), so the TWIAB can detect $B = 3$ T of the magnetic induction intensity. According to the outcome in Fig. 10, the general distribution of magnetic induction intensity ranging from 0.1 to 5.3 T can be measured theoretically. Through the simulation of a different distribution of B, the trend of TWIAB in the frequency domain is given in Fig. 11 to express the performance of a wide range of magnetic field detection in the THz region. It can be observed from Fig. 11 that the fitting degrees between B and f are as high as 0.99997, which shows the linearity of f and B is excellent. The corresponding sensitivity is 1.85296 THz/T with an average FOM of about 5.58 T^{-1}. After the above discussions on TWIAB and the detection of B with the detailed data shown in Table IV, the proposed overall structure has the characteristics of ultra-wide magnetic field detection range and high linearity, which is of great effectivity for the application in magnetic field detection and possesses unique coexistence of transmission and absorptance, especially in the field of military electronic countermeasures.

IV. CONCLUSION

In summary, a multiphysical quantity measurable sensor for the detection of magnetic and temperature fields is designed based on the characteristic of APITB. The properties of APITB are theoretically calculated by TMM and the effects of B and

Te are also studied. The results show that when TM wave propagates in cell structure at $\theta = 82°$, the phenomenon of AWTB can be found. The absorption peak of APITB is blue-shifted as B and Te are increased, and the measurements of its sensing performance are 1.519 THz/T and 0.081 THz/K for magnetic field and temperature. Moreover, an ultra-wideband absorption (3.27–10.06 THz) can be achieved in the whole structure and TWIAB with different distributions by defining external B functions. Through the analysis of the sensing performance of TWIAB generated by different magnetic field distributions, the wide range of magnetic induction intensity (from 0.6 to 5.1 T) in the THz region can be detected with a sensitivity of 1.85296 THz/T. These results offer novel ideas for THz sensors with the measurement of multiple physical quantities and the coexisting absorption–transmission conversion.

REFERENCES

[1] A. R. M. Zain, N. P. Johnson, M. Sorel, and R. M. D. L. Rue, "Ultra high quality factor one dimensional photonic crystal/photonic wire micro-cavities in silicon-on-insulator (SOI)," *Opt. Exp.*, vol. 16, no. 16, pp. 12084–12089, Aug. 2008.

[2] G. Tang, X. He, F. Shi, J. Liu, X. Chen, and J. Dong, "Topological photonic crystals: Physics, designs, and applications," *Laser Photon. Rev.*, vol. 16, no. 4, Feb. 2022, Art. no. 2100300.

[3] J.-W. Gao, J.-H. Wu, N. Ba, C.-L. Cui, and X.-X. Tian, "Efficient all-optical routing using dynamically induced transparency windows and photonic band gaps," *Phys. Rev. A, Gen. Phys.*, vol. 81, no. 1, Jan. 2010, Art. no. 013804.

[4] M. Notomi, "Theory of light propagation in strongly modulated photonic crystals: Refractionlike behavior in the vicinity of the photonic band gap," *Phys. Rev. B, Condens. Matter*, vol. 62, no. 16, pp. 10696–10705, Oct. 2000.

[5] K. Fang, Z. Yu, V. Liu, and S. Fan, "Ultracompact nonreciprocal optical isolator based on guided resonance in a magneto-optical photonic crystal slab," *Opt. Lett.*, vol. 36, no. 21, pp. 4254–4256, Nov. 2011.

[6] Y. Yu, Y. Chen, H. Hu, W. Xue, K. Yvind, and J. Mork, "Nonreciprocal transmission in a nonlinear photonic-crystal Fano structure with broken symmetry," *Laser Photon. Rev.*, vol. 9, no. 2, pp. 241–247, Mar. 2015.

[7] E. Cassan, K. V. Do, J. Dellinger, X. L. Roux, F. Fornel, and B. Cluzel, "Polarization beam splitting using a birefringent graded photonic crystal," *Opt. Lett.*, vol. 38, no. 4, pp. 459–461, Feb. 2013.

[8] N. Gómez-Cardona, C. Jiménez-Durango, J. Usuga-Restrepo, P. Torres, and E. Reyes-Vera, "Thermo-optically tunable polarization beam splitter based on selectively gold-filled dual-core photonic crystal fiber with integrated electrodes," *Opt. Quantum Electron.*, vol. 53, no. 2, pp. 1–15, Jan. 2021.

[9] X. Wang, Y. Liang, L. Wu, J. Guo, X. Dai, and Y. Xiang, "Multi-channel perfect absorber based on a one-dimensional topological photonic crystal heterostructure with graphene," *Opt. Lett.*, vol. 43, no. 17, p. 4256, Sep. 2018.

[10] Y. Yu and H. Da, "Broadband and perfect absorption of monolayer MoS$_2$ with Octonacci quasi-photonic crystal," *Phys. B, Condens. Matter*, vol. 604, Mar. 2021, Art. no. 412684.

[11] C. Liu et al., "Surface plasmon resonance (SPR) infrared sensor based on D-shape photonic crystal fibers with ITO coatings," *Opt. Commun.*, vol. 464, Jun. 2020, Art. no. 125496.

[12] W. Luo, X. Li, J. Meng, Y. Wang, and X. Hong, "Surface plasmon resonance sensor based on side-polished D-shaped photonic crystal fiber with split cladding air holes," *IEEE Trans. Instrum. Meas.*, vol. 70, 2021, Art. no. 7002411.

[13] A. Natesan, K. P. Govindasamy, T. R. Gopal, V. Dhasarathan, and A. H. Aly, "Tricore photonic crystal fibre based refractive index sensor for glucose detection," *IET Optoelectron.*, vol. 13, no. 3, pp. 118–123, Jun. 2019.

[14] N. Ayyanar, G. T. Raja, M. Sharma, and D. S. Kumar, "Photonic crystal fiber-based refractive index sensor for early detection of cancer," *IEEE Sensors J.*, vol. 18, no. 17, pp. 7093–7099, Sep. 2018.

[15] H. K. Baghbadorani and J. Barvestani, "Sensing improvement of 1D photonic crystal sensors by hybridization of defect and Bloch surface modes," *Appl. Surf. Sci.*, vol. 537, Jan. 2021, Art. no. 147730.

[16] S. Elshahat, I. Abood, M. S. M. Esmail, Z. B. Ouyang, and C. C. Lu, "One-dimensional topological photonic crystal mirror heterostructure for sensing," *Nanomaterials*, vol. 11, no. 8, pp. 1–9, Jul. 2021.

[17] A. M. Ahmed, H. A. Elsayed, and A. Mehaney, "High-performance temperature sensor based on one-dimensional pyroelectric photonic crystals comprising Tamm/Fano resonances," *Plasmonics*, vol. 16, no. 2, pp. 547–557, Nov. 2020.

[18] A. M. Ahmed and A. Mehaney, "Novel design of wide temperature ranges sensor based on Tamm state in a pyroelectric photonic crystal with high sensitivity," *Phys. E, Low-Dimensional Syst. Nanostruct.*, vol. 125, Jan. 2021, Art. no. 114387.

[19] X. Yan, R. Fu, T. Cheng, and S. Li, "A highly sensitive refractive index sensor based on a V-shaped photonic crystal fiber with a high refractive index range," *Sensors*, vol. 21, no. 11, p. 3782, May 2021.

[20] Z. A. Zaky, A. Sharma, and A. H. Aly, "Tamm plasmon polariton as refractive index sensor excited by gyroid metals/porous Ta_2O_5 photonic crystal," *Plasmonics*, vol. 17, no. 2, pp. 681–691, Oct. 2021.

[21] C. Zhang, S. Pu, Z. Hao, B. Wang, M. Yuan, and Y. Zhang, "Magnetic field sensing based on whispering gallery mode with nanostructured magnetic fluid-infiltrated photonic crystal fiber," *Nanomaterials*, vol. 12, no. 5, p. 862, Mar. 2022.

[22] D. Ge, H. Chen, P. Jin, L. Zhang, W. Li, and J. Jiao, "Magnetic field sensor based on evanescent wave coupling effect of photonic crystal slab microcavity," *J. Magn. Magn. Mater.*, vol. 527, Jun. 2021, Art. no. 167696.

[23] N. R. Ramanujam, H. J. El-Khozondar, V. Dhasarathan, S. A. Taya, and A. H. Aly, "Design of one dimensional defect based photonic crystal by composited superconducting material for bio sensing applications," *Phys. B, Condens. Matter*, vol. 572, pp. 42–55, Nov. 2019.

[24] A. H. Aly and Z. A. Zaky, "Ultra-sensitive photonic crystal cancer cells sensor with a high-quality factor," *Cryogenics*, vol. 104, Dec. 2019, Art. no. 102991.

[25] I. S. Amiri et al., "Tri-core photonic crystal fiber based refractive index dual sensor for salinity and temperature detection," *Microw. Opt. Technol. Lett.*, vol. 61, no. 3, pp. 847–852, Mar. 2019.

[26] B.-F. Wan, Y. Xu, Z.-W. Zhou, D. Zhang, and H.-F. Zhang, "Theoretical investigation of a sensor based on one-dimensional photonic crystals to measure four physical quantities," *IEEE Sensors J.*, vol. 21, no. 3, pp. 2846–2853, Feb. 2021.

[27] Y. Ma, T. Zhang, M. Y. Mao, D. Zhang, and H. F. Zhang, "Switchable multifunctional modulator realized by the stacked graphene-based hyperbolic metamaterial unit cells," *Opt. Exp.*, vol. 28, no. 26, pp. 39890–39903, Dec. 2020.

[28] S. K. Awasthi, R. Panda, P. K. Chauhan, and L. Shiveshwari, "Multichannel tunable omnidirectional photonic band gaps of 1D ternary photonic crystal containing magnetized cold plasma," *Phys. Plasmas*, vol. 25, no. 5, May 2018, Art. no. 052103.

[29] E. Rangel et al., "Interplay of cavity thickness and metal absorption in thin-film InGaN photonic crystal light-emitting diodes," *Appl. Phys. Lett.*, vol. 97, no. 6, Aug. 2010, Art. no. 061118.

[30] K. Chen et al., "Graphene photonic crystal fibre with strong and tunable light-matter interaction," *Nature Photon.*, vol. 13, no. 11, pp. 754–759, Aug. 2019.

[31] A. H. Aly and D. Mohamed, "BSCCO/$SrTiO_3$ one dimensional superconducting photonic crystal for many applications," *J. Supercond. Novel Magn.*, vol. 28, no. 6, pp. 1699–1703, Feb. 2015.

[32] H.-Y. Ryu, H.-G. Park, and Y.-H. Lee, "Two-dimensional photonic crystal semiconductor lasers: Computational design, fabrication, and characterization," *IEEE J. Sel. Topics Quantum Electron.*, vol. 8, no. 4, pp. 891–908, Jul. 2002.

[33] T. C. King, Z. H. Huang, C. H. Hung, and C. J. Wu, "Investigation of one-way absorption properties in an asymmetric photonic crystal containing a semiconductor defect," *Appl. Opt.*, vol. 57, no. 12, pp. 3115–3118, Apr. 2018.

[34] S. Ghafari, M. R. Forouzeshfard, and Z. Vafapour, "Thermo optical switching and sensing applications of an infrared metamaterial," *IEEE Sensors J.*, vol. 20, no. 6, pp. 3235–3241, Mar. 2020.

[35] L. Qi, Z. Yang, F. Lan, X. Gao, and Z. Shi, "Properties of obliquely incident electromagnetic wave in one-dimensional magnetized plasma photonic crystals," *Phys. Plasmas*, vol. 17, no. 4, Apr. 2010, Art. no. 042501.

[36] S. Chen, F. Fan, X. Wang, P. Wu, H. Zhang, and S. Chang, "Terahertz isolator based on nonreciprocal magneto-metasurface," *Opt. Exp.*, vol. 23, no. 2, p. 1015, Jan. 2015.

[37] V. I. Belotelov and A. K. Zvezdin, "Magneto-optical properties of photonic crystals," *J. Opt. Soc. Amer. B, Opt. Phys.*, vol. 22, no. 1, pp. 286–292, Jan. 2005.

[38] H.-F. Zhang, S.-B. Liu, and Y.-J. Tang, "The properties of the extraordinary mode and surface plasmon modes in the three-dimensional magnetized plasma photonic crystals based on the magneto-optical Voigt effects," *Phys. Plasmas*, vol. 21, no. 6, Jun. 2014, Art. no. 062115.

[39] C. Guclu, S. Campione, and F. Capolino, "Hyperbolic metamaterial as super absorber for scattered fields generated at its surface," *Phys. Rev. B, Condens. Matter*, vol. 86, no. 20, Nov. 2012, Art. no. 205130.

[40] Q. Liu, S. Li, H. Chen, Z. Fan, and J. Li, "Photonic crystal fiber temperature sensor based on coupling between liquid-core mode and defect mode," *IEEE Photon. J.*, vol. 7, no. 2, Apr. 2015, Art. no. 4500509.

[41] H. Huang et al., "A highly magnetic field sensitive photonic crystal fiber based on surface plasmon resonance," *Sensors*, vol. 20, no. 18, p. 5193, Sep. 2020.

[42] Y. Zhao, D. Wu, R.-Q. Lv, and J. Li, "Magnetic field measurement based on the Sagnac interferometer with a ferrofluid-filled high-birefringence photonic crystal fiber," *IEEE Trans. Instrum. Meas.*, vol. 65, no. 6, pp. 1503–1507, Jun. 2016.

[43] M. Shi, S. Li, and H. Chen, "A high-sensitivity temperature sensor based on Sagnac interferometer employing photonic crystal fiber fully filled with ethanol," *Appl. Phys. B, Lasers Opt.*, vol. 124, no. 6, pp. 1–7, May 2018.

[44] M. A. Mollah, S. M. R. Islam, M. Yousufali, L. F. Abdulrazak, M. B. Hossain, and I. S. Amiri, "Plasmonic temperature sensor using D-shaped photonic crystal fiber," *Results Phys.*, vol. 16, Mar. 2020, Art. no. 102966.

[45] Y. E. Monfared, C. Liang, R. Khosravi, B. Kacerovska, and S. Yang, "Selectively toluene-filled photonic crystal fiber Sagnac interferometer with high sensitivity for temperature sensing applications," *Results Phys.*, vol. 13, Jun. 2019, Art. no. 102297.

Tao Zhang was born in Jiangsu, China, in 1999. He is currently pursuing the master's degree with the Nanjing University of Posts and Telecommunications, Nanjing, China.

His main research interests include Goos–Hänchen shift, faraday rotation, and fano resonances.

Yu Ma was born in Henan, China, in 1995. He is currently pursuing the master's degree with the Nanjing University of Posts and Telecommunications, Nanjing, China.

His main research interests include nanophotonics, graphene, and metamaterials.

Hai-Feng Zhang was born in Jiangxi, China, in 1978. He received the M.Sc. degree in electronics science and technology from Nanchang University, Nanchang, China, in 2008, and the Ph.D. degree from the College of Electronic and Information Engineering, Nanjing University of Aeronautics and Astronautics, Nanjing, China, in 2014.

He is currently working as a Professor with the College of Electronic and Optical Engineering and College of Flexible Electronics (Future Technology), Nanjing University of Posts and Telecommunications, Nanjing. His main research interests include computational electromagnetics, plasma photonic crystal, plasma stealthy, and electromagnetic properties of metamaterials.